

Optical Engineering

SPIDigitalLibrary.org/oe

Development of an integrated narrowband tunable filter for LIDAR applications

Dionísio Alves Pereira
Francisco Manuel Moita Araújo
Luís Alberto de Almeida Ferreira
José Luís Santos
Manuel B. Marques
João Pedro Carmo

Development of an integrated narrowband tunable filter for LIDAR applications

Dionísio Alves Pereira

University of Porto
Physics Department
Rua do Campo Alegre
4169-007 Porto
Portugal
and
INESC
Porto Optoelectronics and Electronics
Systems Unit
Rua do Campo Alegre
687 4150-179 Porto
Portugal
E-mail: dionisioalvespereira@gmail.com

Francisco Manuel Moita Araújo Luís Alberto de Almeida Ferreira

INESC
Porto Optoelectronics and Electronics
Systems Unit
Rua do Campo Alegre
687 4150-179 Porto
Portugal

José Luís Santos Manuel B. Marques

University of Porto
Physics Department
Rua do Campo Alegre
4169-007 Porto
Portugal
and
INESC
Porto Optoelectronics and Electronics
Systems Unit
Rua do Campo Alegre
687 4150-179 Porto
Portugal

João Pedro Carmo

ESTEC
Keplarlaan 1
P.O. Box 299
2200 AG Noordwijk ZH
The Netherlands

1 Introduction

A wide range of solutions employing fiber Bragg grating (FBG) fabrication have been proposed recently for advanced optical filtering functionality, including FBG-based ultranarrow filters.¹⁻³ A good example of this option can be found in dense wavelength division multiplexing systems where, in order to isolate bands and reduce cross-talk between adjacent channels, ultranarrow optical filtering is required. In

Abstract. The overall procedure toward the implementation of a compact tunable athermal filter mounted on a piezoelectric actuator and based on a π -shift chirped fiber Bragg grating is presented. This package ensures an active tunability over 2 nm with a cross thermal induced Bragg wavelength shift below 100 pm over a temperature range from -20°C to $+80^{\circ}\text{C}$. The proposed filter makes use of the overall response of a π -shift chirped fiber Bragg grating and a bulk broadband microfilter that enables a sharp optical transmission spectrum response having a FWHM below 20 pm within a 2 nm region and 20 dB rejection band to be obtained. © 2011 Society of Photo-Optical Instrumentation Engineers (SPIE). [DOI: 10.1117/1.3656751]

Subject terms: fiber optic sensors; tunable filters; LIDAR.

Paper 110922R received Aug. 2, 2011; revised manuscript received Sep. 28, 2011; accepted for publication Oct. 10, 2011; published online Nov. 17, 2011.

a distinct domain, these filters can also be adapted for use as sharp frequency discriminators in a laser linewidth reduction system,⁴ or inside a fiber laser scheme suitable for use in sensing applications.⁵ The filter proposed in this paper extends the range of applications to one of special interest: LIDAR (light detection and ranging).⁶

Strictly speaking, LIDAR is a methodology commonly used for atmospheric gas scanning and monitoring that is based on the analysis of the light backscattered by the atmosphere, when illuminated by a laser pulse. In general, processing of the reflected radiation signal, that is essentially

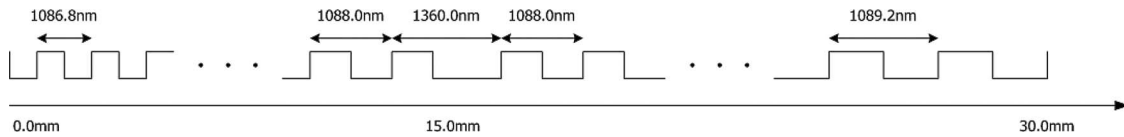


Fig. 1 Illustration of the design specifications of the custom phase mask.

due to Rayleigh and Mie scattering mechanisms, demands the design of feasible and precise optical techniques which, together with sophisticated apparatus, enable to collect and separate the signal from the background noise.

The filter here proposed was planned to be an alternative and advantageous all-fiber solution for signal-filtering and is based on the combined optical transmission response of a bulk micro-optical filter and a π -shift chirped FBG with an exceptional sharp peak response. As a consequence, when compared to multilayer thin-films or even to their optical fiber counterparts, Fabry–Perot and ring-resonator,^{7,8} it significantly reduces the passband. In the scope of LIDAR applications, of particular interest is its ability to spectrally resolve the fine structure of a gas absorption spectrum. Essentially, the narrow response of the filter proposed here was only made possible due to the modern phase-shift chirped phase masks manufacturing processes. These processes enable filters with extremely narrow transmission resonances within an FBG broad rejection band to be produced. For this reason, and in order to achieve maximum repeatability during the writing process, a tailored chirped π -shift phase mask was used in preference to the phase-mask dithering technique.

A recursive problem associated with optical fiber-based filters is their susceptibility to external thermal variations that affect their response and lead to errors in measurements. To overcome this limitation, the implemented filter package ensures athermal operation for external temperature variations in extent of 100°C which largely exceeds routine temperature variations experienced on earth by LIDAR systems. The grating was mounted in a piezoelectric actuator that allows filter central spectral response to be fine tuned within a range of 2 nm.

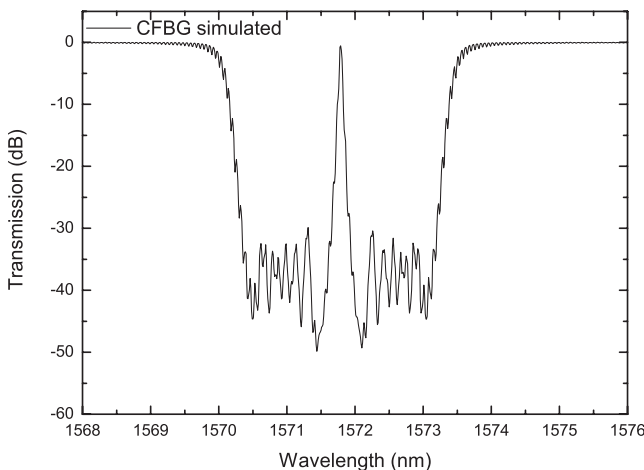


Fig. 2 Lossless simulated π -shift CFBG.

2 Experiments and Results

2.1 Phase-Mask Design

The well-known transfer-matrix model for simulation of fiber Bragg gratings is an elegant mathematical tool for the determination of any arbitrary phase-shift in the FBG final spectrum.⁹ This method was used to simulate the response of the π -shift chirped FBG, with a narrow transmission notch over a broadband rejection. In particular, when a precise half-period π -shift FBG is the target, a $\Lambda_\phi = \Lambda/4$ step is printed in the phase-mask pattern of spatial period Λ . The specifications used for the phase-shift chirped phase mask design are illustrated in Fig. 1. In essence it includes: phase mask period at initial position of 1086.8 nm; a chirp rate of 0.8 nm/cm; a phase shift step at central position of 272 nm; and a phase mask length of 30 mm. The central wavelength was selected to target the CO₂ absorption band around 1572 nm. This phase-mask was used for manufacturing the π -shift chirped fiber Bragg grating (CFBG).

2.2 Simulation of the Global Filter Spectral Response and CFBG Fabrication

As mentioned in Sec. 1, the proposed filter scheme has two optical components: a phase-shift CFBG and a bulk broadband rejection microfilter. Prior to grating fabrication, the expected spectral combined response was evaluated from its individual spectral responses. Figures 2 and 3 show the individual spectral responses of an ideal lossless CFBG obtained using the transfer-matrix method and of the broadband rejection filter, respectively.

Figure 4 shows the combined spectral response of the filter and, for a comprehensive reading, the absorption spectral lines of a CO₂ gas cell. This scheme results in an ultranarrow

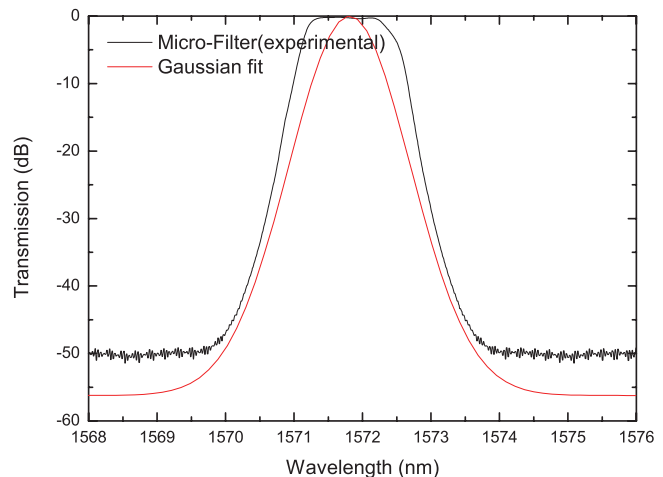


Fig. 3 Microfilter transmission.

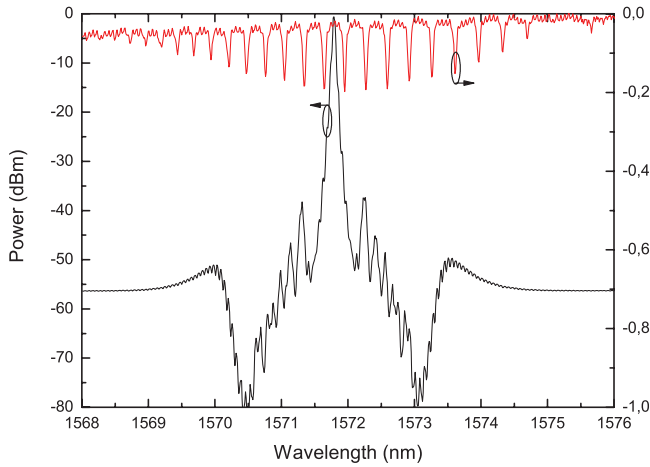


Fig. 4 Simulated filter-transfer-function and measured CO₂ absorption spectral lines (upper-trace).

transmission line, corresponding to the central resonance peak of the phase-shift CFBG, while providing a broadband rejection of the background radiation.

An interesting point to notice when CFBGs are fabricated is their asymmetrical reflection spectrum when illuminated from each end.¹⁰ This behavior, which is comprehensible given the cladding modes associated loss mechanism observed during UV exposure, creates a gradual and continuous asymmetry of the reflection spectral response.¹¹ Although the impact of such a loss being negligible in filters performance, due to the negligible influence on the transmission response, its effect is visible in the left side of the simulation addressed in Fig. 5 and for this reason is mentioned here.

The π -shift CFBG simulated and experimental spectra shown in Figs. 5 and 6 agree. The difference observed in the central peak depth results from a limitation of the adopted method for the simulation which for simplicity is a hybrid model that uses coupled mode equations and the transfer matrix model. For the CFBG fabrication, we used Corning SMF-28 fiber previously hydrogen loaded at 150 bar during 15 days and a continuous-wave Gaussian UV beam, with 50 mW of power focused on a $\sim 200 \mu\text{m}$ diameter spot. The scanning speed was $v = 0.015 \mu\text{ms}^{-1}$. The experimental spectral width (FWHM) of the resonant transmission peak,

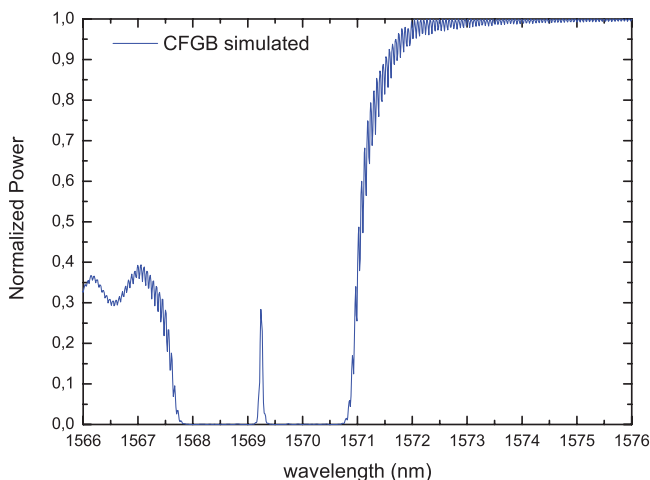


Fig. 5 Simulated π -shift CFBG spectrum.

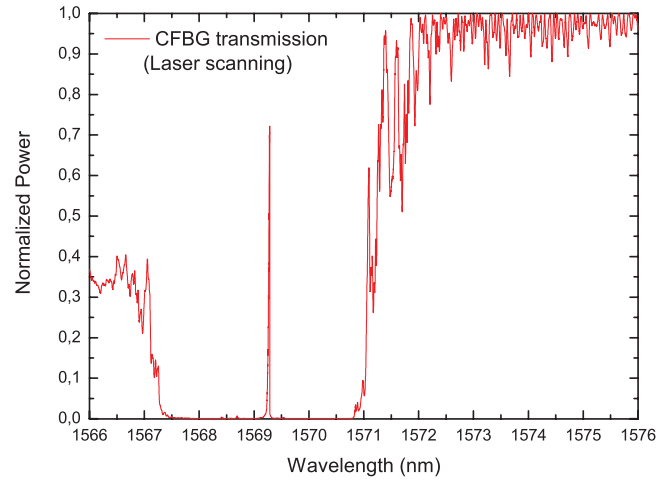


Fig. 6 Experimental π -shift CFBG spectrum.

20 pm, is consistent with the values quoted in the literature for use of ultranarrow band filter in gas monitoring and LIDAR water vapor measurements.¹²

2.3 FBG Athermal Model

It is well known that thermal effects in fiber optic filters are typically an order of magnitude higher than in air-path counterparts, leading inevitably to cross talk in spectral measurements. Without any loss of generality the analysis needed to describe the FBG peak variation when submitted to a temperature variation ΔT and strain variation $\Delta \epsilon$ is greatly simplified if one considers linear temperature and strain dependences. Accordingly, for a temperature variation ΔT , and considering the fiber free from any external loading, the FBG wavelength shift of period Λ and effective refractive index n can be expressed in the following manner:¹³

$$\begin{aligned} \Delta \lambda_B &= \lambda_B \left(\frac{1}{\Lambda} \frac{\partial \Lambda}{\partial T} + \frac{1}{n} \frac{\partial n}{\partial T} \right) \Delta T = \lambda_B (\alpha + \xi) \Delta T \\ &= \lambda_B \beta_T \Delta T. \end{aligned} \quad (1)$$

The parameter α is the fiber coefficient of thermal-expansion (CTE), β_T is the optical fiber thermal sensitivity, and ξ is the fiber thermo-optic coefficient, with values of 0.55 and 6.7 ppm/ $^\circ\text{C}$, respectively.^{14,15} Similarly, in the case of the FBG being subjected to longitudinal strain ϵ and in the absence of any external temperature variation ΔT , the corresponding wavelength shift is given by

$$\Delta \lambda_B = \lambda_B \left(\frac{1}{\Lambda} \frac{\partial \Lambda}{\partial \epsilon} + \frac{1}{n} \frac{\partial n}{\partial \epsilon} \right) \epsilon = \lambda_B (1 - p_\epsilon) \epsilon = \lambda_B \beta_\epsilon \epsilon, \quad (2)$$

where p_ϵ is the optical fiber photoelastic coefficient and β_ϵ is the optical fiber strain sensitivity. The proposed method for attaining athermal operation relies on subjecting the FBG to additional temperature induced strain, $\epsilon(T)$, exactly balancing its intrinsic thermal sensitivity. The complete thermal compensation then imposes that

$$\beta_T + \frac{\beta_\epsilon \epsilon(T)}{\Delta T} = 0. \quad (3)$$

The simplest method of applying temperature dependent strain to a FBG is to attach it to a material with a CTE

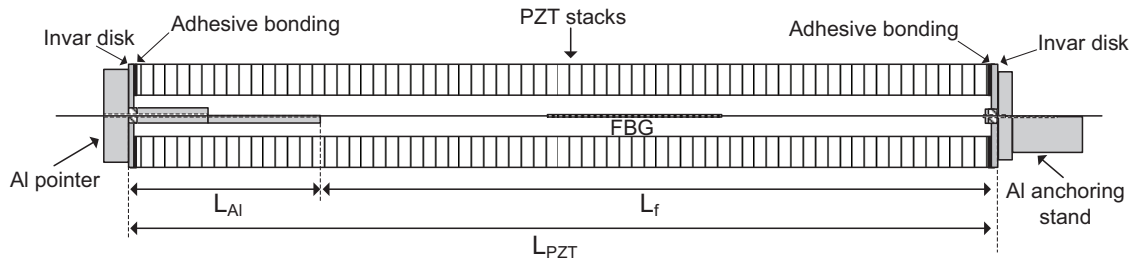


Fig. 7 Schematic representation of the tunable athermal package (longitudinal cut view).

dissimilar to silica. However, this restricts the adjustment of the FBG sensitivity to the set of discrete values that can be obtained employing available materials. A well-known method of attaining a broad range of effective CTE—including negative CTE values—is to provide a structure incorporating a proper arrangement of two materials with distinct CTE values. A proper design of such a structure can be used for packaging FBG filters, allowing for continuous adjustment of the FBG temperature sensitivity.

2.4 Tunable Athermal Package Design

This section describes the features of the proposed tunable athermal package design which combines aluminum and ceramic piezoelectric material. The package contrasts with some of the most common arrangements for athermal packages that are based on the principle described by Morey and Clomb and that combine two metals with distinct CTE.¹⁶

A cut-view of the proposed assembly for the implementation of the fiber Bragg grating tunable athermal package is shown in Fig. 7. The package is composed of an aluminum pointer with length L_{AL} and an aluminum anchoring stand assembled at the ends of a ceramic piezoelectric transducer (PZT) actuator with length L_{PZT} . The fiber is pretensioned and adhesive bonded to the grooves machined in the aluminum pointer and stand, setting a distance L_f between the anchorage points. As illustrated in Fig. 7, two invar disks, with the same cross-section as the PZT actuator, were adhesive-bonded to the ends of the PZT stack. These disks act as a thermal buffer between the PZT ceramic and

the aluminum parts, while their low CTE and small size make their contribution negligible to the global performance of the athermal package. A hollow cylindrical PZT stack was used to ensure tunability, while offering excellent overall mechanical protection for the packaged FBG.

Athermal performance is effectively achieved since, under a temperature increase/decrease, the net strain decrease/increase in the FBG caused by the aluminum pointer higher CTE relatively to the PZT lower CTE perfectly balances the effect of the thermo-optic coefficient of the fiber. Equation (4) discriminates the effects of the thermo-optic coefficient of the fiber, the CTE of the aluminum pointer, and the CTE of the PZT actuator on the thermal induced resonant peak shift of the packaged FBG.

$$\frac{\Delta\lambda_B}{\lambda_B} = \left[\beta_T + \beta_\epsilon \left(-\frac{\alpha_{Al}L_{Al}}{L_{PZT} - L_{Al}} \right) + \beta_\epsilon \left(\frac{\alpha_{PZT}L_{PZT}}{L_{PZT} - L_{Al}} \right) \right] \Delta T. \quad (4)$$

According to Eq. (4), the contributions of the CTE of the PZT actuator to the fiber net tension is positive, since it increases the resonant wavelength when subjected to a temperature increase, whereas the contribution from the aluminum pointer is negative, since it relaxes the fiber when subjected to a positive temperature variation ΔT . The analysis of Eq. (4) immediately suggests that establishing the optimum L_{PZT}/L_{Al} ratio that ensures athermal operation is straightforward once all material and dimensional parameters are set.

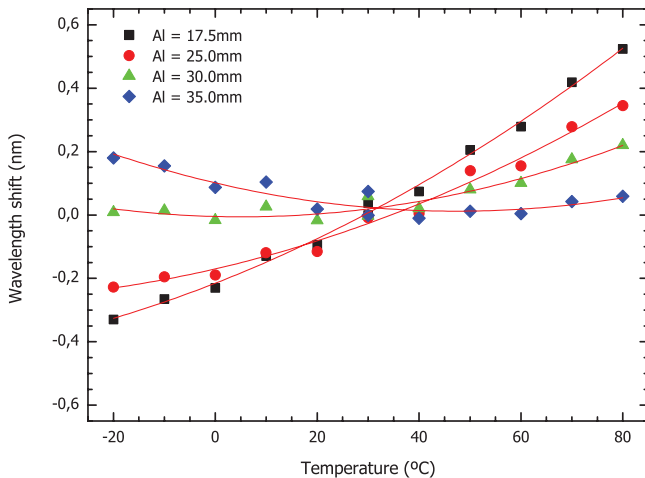


Fig. 8 Tunable athermal package performance for different balancing ratios assembled with PI-PZT actuator.

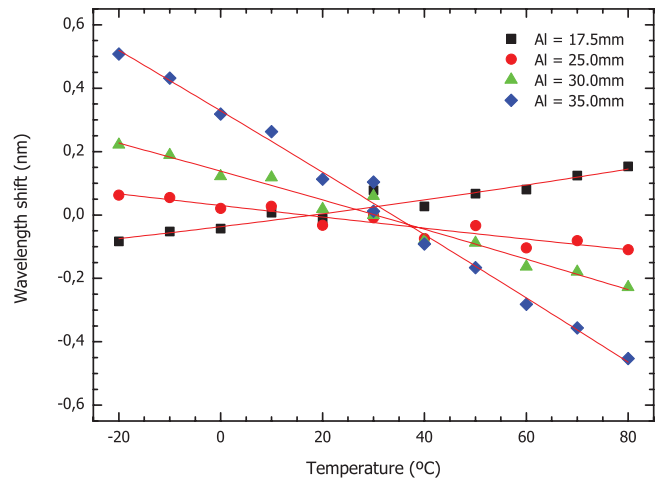


Fig. 9 Tunable athermal package performance for different balancing ratios assembled with Noliac-PZT actuator.

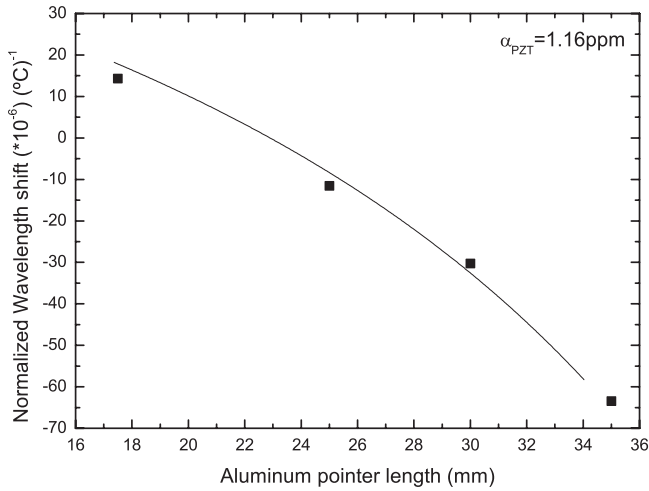


Fig. 10 Normalized athermal package performance as a function of the aluminum pointer length.

2.5 Tunable Athermal Package Tests

The results obtained throughout optimization of the athermal package balance are presented here. Due to the absence of reliable data relative to the CTE value of piezoelectric actuators, it was decided to test PZT actuators from two distinct manufacturers: Noliac A/S (NL-PZT) and Physik Instrumente (PI-PZT). The samples of the tunable athermal packages were subjected to a full thermal cycle with 12 h duration at step intervals of constant temperature of 1 h, beginning at 30°C and increasing at 20°C step up to 70°C and a 10°C step up to 80°C and afterwards decreasing at 20°C step down to -20°C and then increasing a 10°C step up to -10°C and back to the initial temperature 30°C at step up of 20°C. The thermal tests were accomplished for a set of different L_{PZT}/L_{Al} ratios by mounting aluminum pointers with increasing length on the two samples of the PZT actuators mentioned previously. It must be emphasized that throughout all thermal tests, the PZT electrical terminals were shunted to prevent any residual voltage from being generated. The wavelength shift was measured using a FS4200 BraggMETER from FiberSens-

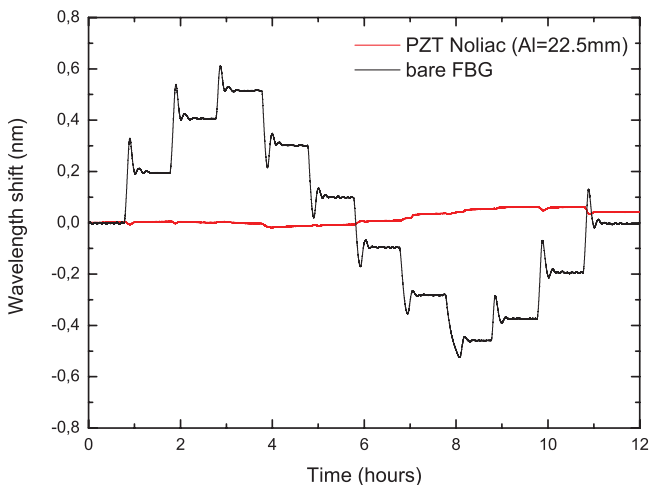


Fig. 11 Athermal package performance during thermal-cycle.

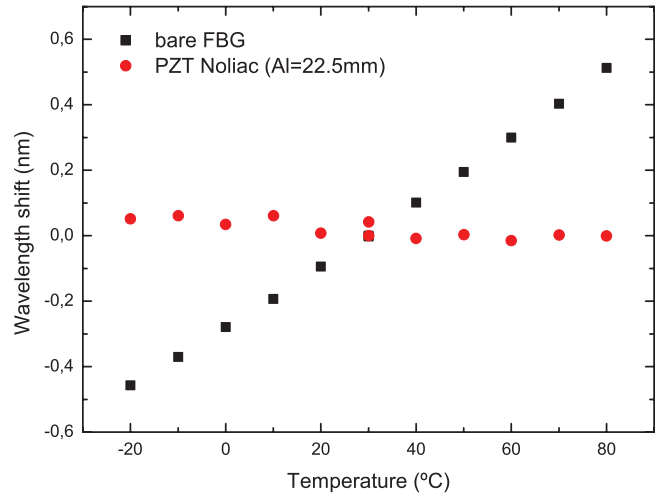


Fig. 12 Athermal package performance for optimum balancing ratio.

ing at a rate of one sample per second. After temperature stabilization within each step, the average wavelength shift was determined with approximately one thousand points. Figures 8 and 9 present the results of the average resonant FBG wavelength shift for aluminum pointers with different length for PI and Noliac PZT actuators, respectively. The results exhibit a noticeable difference in the overall behavior of FBGs assembled on packages based on the two distinct PZT actuators, when hosting aluminum pointers of identical length. Indeed, while the PI-PZT evidences a significant nonlinear thermal dependence, the NL-PZT sample presents an almost linear response. Data in Figs. 8 and 9 can be analyzed from smaller to longer aluminum pointer, making the balancing length for which the slope inversion occurs clearly perceptible.

The analysis of data presented in Figs. 8 and 9 reveal that the slope inversion occurs on the lower vicinity of aluminum pointers with 35 and 25 mm length for PI-PZT and Noliac-PZT actuators, respectively. From data displayed in the graphs above, and through Eq. (4), the thermal expansion coefficient of the PZTs can be estimated. For this calculation, the values used for the parameters β_ϵ and β_T in the 1.5 μm region were 5.6 ppm/°C and 0.76 ppm/ $\mu\epsilon$,¹⁴ respectively.

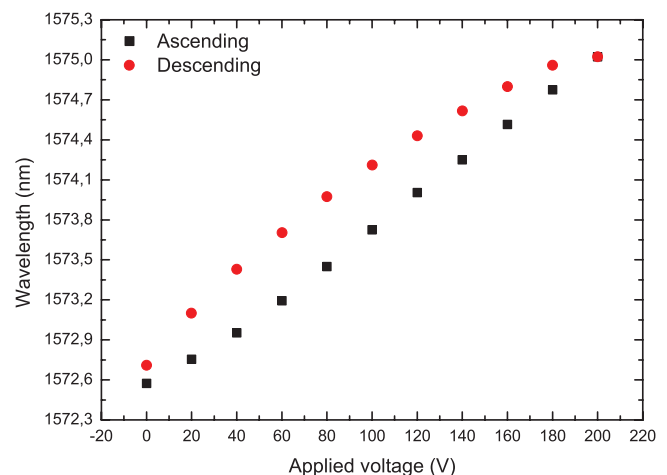


Fig. 13 Filter-tuning.

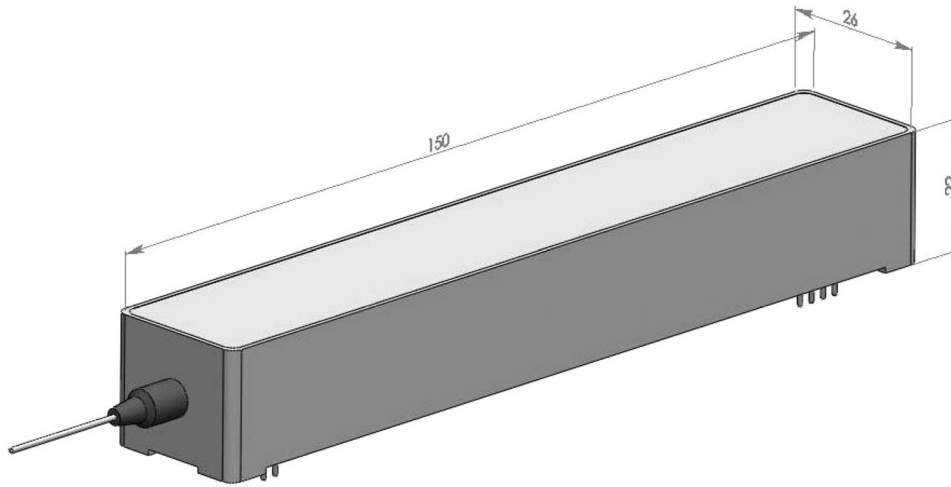


Fig. 14 Outside package view.

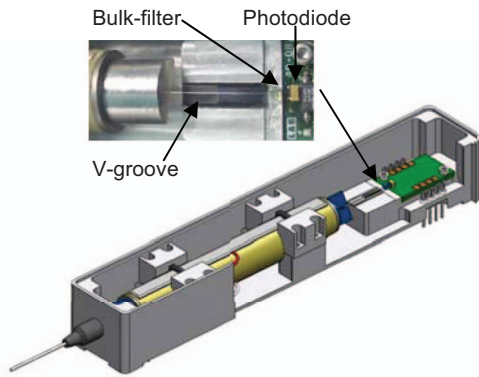


Fig. 15 Mechanical CAD drawing of the integrated micro-optic filter. Inset photo shows the fiber alignment with bulk-filter and photodetector.

The value of β_T differs from the standard value quoted in the literature because the FBG is bonded to the package, which prevents it from expanding or contracting. This is equivalent to setting $\alpha = 0$ in Eq. (1). The value used for the aluminum CTE was $23.5 \text{ ppm}/^\circ\text{C}$. Linear polynomial fit was used for the NL-PZT, while in the case of the PI-PZT a second order polynomial adjustment was used. Still, due to the relative magnitude of the linear and quadratic terms, only the linear term was considered for the calculations. The CTE values were then estimated by fitting Eq. (4) to the data points while the parameter α_{PZT} was left free in the fitting process. The estimation of the CTE of the PZT actuators, $1.7 \text{ ppm}/^\circ\text{C}$ for NL-PZT and $4.7 \text{ ppm}/^\circ\text{C}$ for PI-PZT, allows for optimal package design, giving improved thermal compensation. The NL-PZT actuator was selected to implement the final package, since it offers an almost linear thermal dependence for the resonant shift of the packaged FBG and presents a lower CTE value that enables a smaller package to be attained (as the aluminum pointer can be made smaller). The plot of the normalized wavelength shift as a

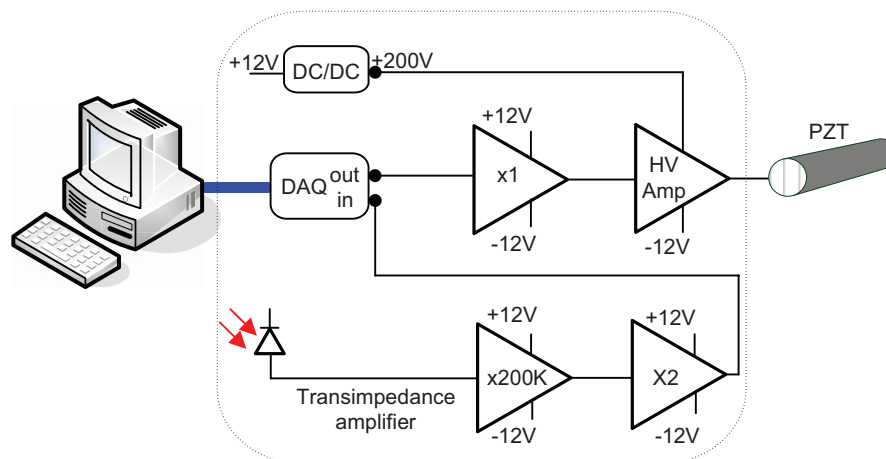


Fig. 16 Electronic block-diagram for signal processing and PZT control.

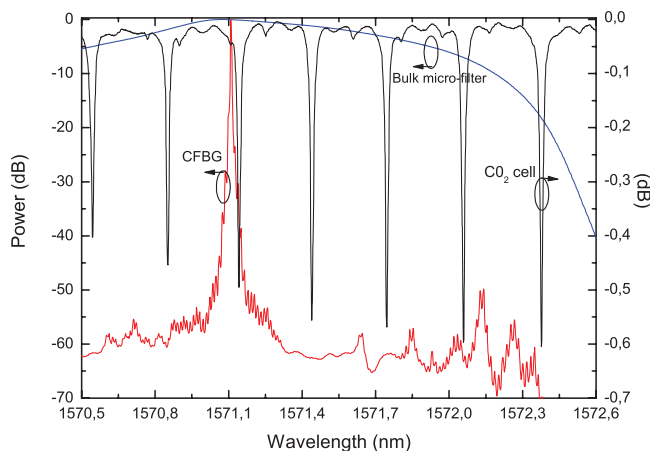


Fig. 17 Close-up of individual filter components response.

function of the aluminum pointer length (see Fig. 10) enables the determination of the exact balancing of the package design using the value estimated for the CTE of the PZT actuator. Fitting this data with Eq. (4) an optimum length for the aluminum pointer of 22.5 mm can be determined.

Figure 11 shows the time dependence of the wavelength shift of a FBG assembled in an athermal package with optimum balance L_{PZT}/L_{Al} ratio, together with a bare unpackaged FBG used as reference during a full thermal cycle. The procedure described above was applied to evaluate the performance of the athermal package (see Fig. 12). It is possible to observe that the packaged FBG has a residual thermal dependence lower than one-tenth of the unpackaged FBG.

Finally, the package was tested for tunability. Data in Fig. 13 shows that the resonant peak of the packaged FBG can be tuned over a 2 nm range for an applied voltage of 200 V. Hysteresis can be observed, as expected, due to the piezoelectric nature of the actuator. It must be pointed out that the proposed scheme not only compensates the intrinsic thermal sensitivity of the FBG filter, but also cancels the effect of the CTE of the PZT actuator. In fact, if the FBG filter was directly bonded to the PZT actuator to achieve tunability, the overall thermal dependence of the device would be amplified by the CTE of the actuator.

2.6 Filter Assembly and Final Testing

Figures 14 and 15 show the final implemented filter package. Figure 15 shows the inner details of the proposed package built up from a customized aluminum case. Inside are the NL-PZT stack, a high precision V-groove in silicon chip, a bulk broadband rejection micro-optic filter, and a photodiode with its corresponding *in situ* photodiode plane circuit board. The V-groove ensures a stable and fine alignment between the optical fiber output and the microfilter which is adhesive bonded in the gap between the fiber output and the photodiode. Also, as visible in Fig. 15, a set of eight pins are inserted in the bottom of the aluminum case just above the photodiode; these pins, together with two others (not visible in Fig. 15), enable integration of the case with an external circuit board for PZT-drive, power supply, and electrical signal transmission.

For the photodiode preamplifier included in the filter packaging a standard transimpedance configuration was chosen

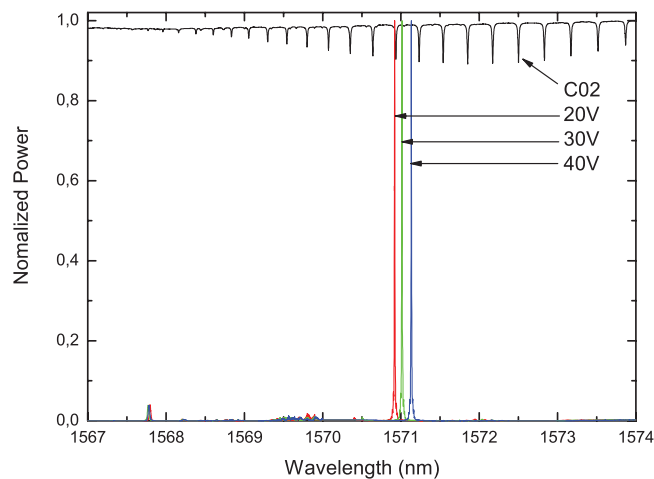


Fig. 18 Experimental characterization of the integrated micro-optic filter Versus carbon-dioxide absorption bands.

first due to its higher sensitivity and second to its advantage for low frequency response applications.¹⁷ This regime, namely the photovoltaic regime of operation, reduces the adverse effects of photodiode dark current, which are detrimental to achieve a large signal-to-noise ratio. The core of the external circuit control board includes two major blocks for PZT tunability: a qualified DC-DC converter that operates over a wide input voltage range while maintaining tight output regulation and a high voltage amplifier carefully selected for its ability to drive high capacitance loads as is the case of the NL-PZT (~ 6300 nF). A simplified diagram block of the processing and conditioning signal electronics board is shown in Fig. 16. Figure 17 shows the filter output spectrum with 1 pm resolution measured with a SANTEC TSL-210 tunable laser source. This result is in clear agreement with the simulation addressed in Fig. 4. As planned, the narrow filter response clearly resolves the CO₂ absorption gas lines, while it is free to be offset and fine tuned for optimum scanning. An illustration of its fine tuning ability is addressed in Fig. 18. Giving the tuning range addressed in Fig. 13, the filter can be tuned in excess, to encompass several absorption gas lines.

3 Conclusions

The filter demonstrated in this paper is a compact and relatively simple device that has the ability to resolve typical gas absorption spectrum lines with typical widths of a few tenths of nanometer. Special attention was given to the CFBG modeling and fabrication techniques, prior to package assembly, which dictates the targeted spectral response of the filter. The proposed filter has a state-of-the-art athermal response in fiber optics-based devices that correspond to a wavelength drift below 10 pm for 100°C of temperature variation. The active tunability of the filter, larger than 2 nm, is enough for the majority of situations where fine tuning of gas lines is required. Due to its construction, single-end optical interface and a small size, this device is very attractive to be incorporated into more complex bulk optics based LIDAR systems for remote gas scanning and monitoring. In those systems, this integrated narrowband filter may act as a core element on the interface between optical incoming radiation and electronic signal for processing.

Acknowledgments

This work was supported in part by the European Space Agency through the project High-Resolution Microoptic Filters for LIDAR Applications, Reference RES-PTM/PA/cpt/569.2005, Subcontract 19622/06/NL/PA in the framework of the ESA-Portugal Task Force. The authors want to thank Weidong Cai and Jean-Jacques Loonis for manufacturing the phase mask.

References

1. E. Turitsyna, R. Bhamber, V. Mezentsev, A. Gillooly, J. Mitchell, and S. Turitsyn, "Design of FBG-based ultra-narrow asymmetric filter for transmission with 0.8 bit/s/Hz spectral efficiency without polarisation multiplexing," *Opt. Fiber Technol.* **11**, 202–208 (2005).
2. W. Liu, S. Lin, C. Cui, J. Shi, L. Zheng, H. Huang, W. Du, Y. Sun, J. Chen, S. B. Lee, and I. H. White, "Dynamic cascaded FBG based filter used in DWDM networks," *Proc. SPIE* **6019**, 60190U (2005).
3. E. Turitsyna and S. Webb, "Simple design of FBG-based VSB filters for ultra-dense WDM transmission," *Electron. Lett.*, **41**(2), 89–91 (2005).
4. J. Cliche, Y. Painchaud, C. Latrasse, M. Picard, I. Alexandre, and M. Titu, "Ultra-narrow Bragg grating for active semiconductor laser linewidth reduction through electrical feedback," in *Bragg Gratings, Photosensitivity, and Poling in Glass Waveguides*, OSA Technical Digest (CD), p. BTuE2, Optical Society of America, Washington, DC (2007).
5. S. Li, N. Ngo, and Z. Zhang, "Tunable fiber laser with ultra-narrow linewidth using a tunable phase-shifted chirped fiber grating," *IEEE Photon. Technol. Lett.* **20**(17), 1482–1484 (2008).
6. R. G. Driggers, *Encyclopedia of Optical Engineering*, Volume 2 of 3, CRC Press, Boca Raton, FL (2003).
7. A. D. Kersey, T. A. Berkoﬀ and W. W. Morey, "Multiplexed fiber Bragg grating strain-sensor system with a fiber Fabry-Perot wavelength filter," *Opt. Lett.* **18**, 1370–1372 (1993).
8. P. Hariharan, "Optical Interferometry," 2nd ed., Academic, New York (2003).
9. T. Erdogan, "Fiber grating spectra," *J. Lightwave Technol.* **15**, 1277–1294 (1997).
10. D. J. Kitcher, A. Nand, S. A. Wade, R. Jones, G. W. Baxter, and S. F. Collins, "Directional dependence of spectra of fiber Bragg gratings due to excess loss," *J. Opt. Soc. Am. A. Opt. Image. Sci. Vis.* **23**, 2906–2911 (2006).
11. T. Erdogan, "Cladding-mode resonances in short- and long-period fiber grating filters," *J. Opt. Soc. Am. A* **14**(8), 1760–1773 (1997).
12. L. B. Vann, R. J. DeYoung, S. J. Mihailov, P. Lu, D. Grobnc, and R. Walker, "Narrowband fiber-optic phase-shifted fabry-perot Bragg grating filters for atmospheric water vapor lidar measurements," *Appl. Opt.* **44**(34), 7371–7377 (2005).
13. Y. Jiang, "In-fibre Bragg grating sensors," *Meas. Sci. Technol.* **8**, 355–375 (1997).
14. A. Kersey, M. Davis, H. Patrick, M. LeBlanc, K. Koo, C. Askins, M. Putnam, and E. Friebele, "Fiber grating sensors," *J. Lightwave Technol.* **15**(8), 1442–1463 (1997).
15. A. Othonos and K. Kalli, *Fiber Bragg Gratings: Fundamentals and Applications in Telecommunications and Sensing*, Artech House Publishers, Boston, MA (1999).
16. W. W. Morey and W. L. Glomb, "Incorporated Bragg filter temperature compensated optical waveguide device," United States Patent 5042898 (1991).
17. J. Graeme, *Photodiode Amplifiers: OP AMP Solutions*, 1st Ed., McGraw-Hill, New York (1995).

Dionísio Alves Pereira graduated in applied physics (lasers and optoelectronics) in 1999 at University of Porto. He joined Optoelectronics and Electronic Systems Unit of INESC Porto in 2001 and received his MSc degree in Optoelectronics in 2003 from the same university. Also from the University of Porto he received his PhD in 2010 in physics for research in fiber grating technology and fiber lasers. During his PhD program, he developed part of the research

work at ORC- Optoelectronics Research Center at Tampere, Finland. Presently he is researcher at Multiwave Photonics.

Francisco Manuel Moita Araújo graduated in applied physics (optics and electronics) from the University of Porto, Portugal. In 1993 he received a PhD degree in physics from the same university in 2000 (fiber Bragg gratings). Presently he is an assistant researcher at the Telecommunications and Multimedia Unit of INESC Porto. His main activity is related with optical communications and fiber optic sensing. Previous positions included leadership of the Fiber Optic Technologies Unit at MultiWave Networks Portugal, a company developing subsystems for fiber optic communications, assistant professor at the Physics Department of the University of Porto (Faculty of Sciences), and senior researcher at the Optoelectronics and Electronic Systems Unit of INESC Porto, where he developed research in the area of fiber optic technologies from 1993 to 2001. He is the author of numerous international communications, papers, and patents in the fields of fiber optic sensing and fiber optic communications.

Luís Alberto de Almeida Ferreira graduated in applied physics (optics and electronics) in 1991 and in 1995 he obtained a MSc degree in optoelectronics and lasers (white-light interferometry and signal processing in optical fiber sensors), both from the University of Porto, Portugal. He received a PhD degree in physics from the same university in 2000 (Interrogation of Fiber Optic Bragg Grating Sensors). During his PhD program, he developed part of the research work in the Physics Department of the University of North Carolina at Charlotte, North Carolina. Presently he is a senior researcher at the Optoelectronics and Electronic Systems Unit of INESC Porto—Institute for Systems and Computer Engineering of Porto. His main activity is related with fiber optic sensing and optical communications. He is a member of the Scientific Council of INESC Porto. He is also a member of the management team, and Sales & Marketing director, of FiberSensing, an INESC Porto spin-off company that he co-founded in 2004. Previous positions included leadership of the Advanced Development Unit at MultiWave Networks Portugal, a company developing subsystems for fibre optic communications, assistant professor at the Physics Department of the University of Porto (Faculty of Sciences), and researcher at the Optoelectronics and Electronic Systems Unit of INESC Porto, where he developed work in the area of fiber optic sensing from 1992 to 2001. He is author/co-author of more than 200 international communications, papers, and patents in the fields of fiber optic sensing and fiber optic communications.

José Luís Santos received a PhD degree in physics for research on fiber-optic sensing at the University of Porto, Portugal, in 1993. He is professor of the Physics and Astronomy Department of University of Porto and researcher of INESC Porto. Member of OSA, SPIE, and Planetary Society.

Manuel B. Marques received a degree in physics from Porto University in 1983, and a PhD degree in physics from the same university in 1991. His thesis work was on nonlinear coupling to optical waveguides. From 1993 to 2001 he was a member of Centro de Física do Porto, where he worked on fiber lasers and integrated optics. He joined INESC Porto, Portugal, in January 2002, where he has worked on fiber lasers and sensors. He has been an assistant professor in the Physics Department of Porto University since 1991. He is a member of the Portuguese Physics Society.

João Pedro Carmo: biography and photograph are not available.